Self-Limiting Electrodeposition of Hierarchical MnO_2 and $M(OH)_2/MnO_2$ Nanofibril/Nanowires: Mechanism and Supercapacitor Properties

Jonathon Duay,[†] Stefanie A. Sherrill,[†] Zhe Gui,[†] Eleanor Gillette,[†] and Sang Bok Lee[†,‡,*]

[†]Department of Chemistry and Biochemistry, University of Maryland, College Park, Maryland 20740, United States, and [‡]Graduate School of Nanoscience and Technology (WCU), Korea Advance Institute of Science and Technology, Daejeon 305-701, Korea

ABSTRACT Hierarchical nanostructures have generated great interest in the energy, materials, and chemical sciences due to the synergic properties of their composite architectures. Herein, a hierarchical MnO_2 nanofibril/nanowire array is successfully synthesized. The structure consists of a conformal layer of MnO_2 nanofibrils evenly distributed on the surface of the individual MnO_2 nanowires. The synthetic mechanism of this hierarchical structure is characterized by electrochemical measurements, Raman spectroscopy, EELS, and electron microscopy. This material was then investigated at slow scan rates for its charge storage mechanisms in different solvents. In aqueous electrolyte, the nanofibrils show a capacitance almost purely dedicated to double-layer and surface adsorption processes, while in an acetonitrile electrolyte, the nanofibrils' capacitance comes mainly from a cation insertion process. This material was also tested at high scan rates in aqueous solution for its practical supercapacitor capabilities. The material shows a large capacitance of 298 F/g at 50 mV/s and 174 F/g at 250 mV/s. It also maintains 85.2% of its capacitance after 1000 cycles. The material also displays easily controllable parameters such as nanowire length, nanowire diameter, and amount of nanofibril material which is shown here to affect the capacitance dramatically.

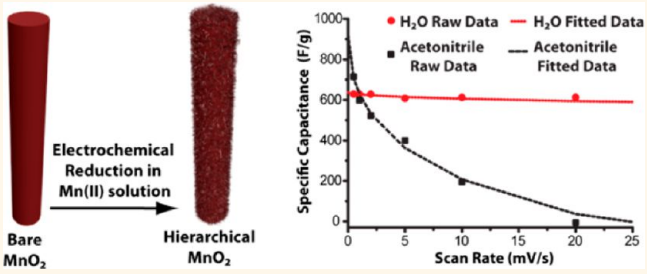

KEYWORDS: hierarchical · nanowires · template · self-limiting · manganese oxide · electrochemical energy storage

It is well-documented that the adsorption, insertion, and conversion reactions associated with catalysis,[1] energy storage,[2,3] energy conversion,[4] chromatography,[5] and chemical sensing[6,7] can be enhanced by using hierarchical nanostructures. This multiscale texturization allows for a synergistic joining of two different length scales. The larger length scale offers an efficient way of transporting the ions (*i.e.*, macropores) or electrons (*i.e.*, one-dimensional structures), while the smaller scale offers either small voids (*i.e.*, micropores) for high ion accessibility with high material density or a higher surface area (*i.e.*, nanoparticles) for greater adsorption or access of ions.

Oxides of manganese (MnO_x) are deeply versatile compounds for material and chemical scientists and are being investigated as important materials for these hierarchical structures.[8−10] MnO_x materials have many favorable qualities that make them desirable products in the chemical science field such as low toxicity, high abundance, low cost, environmental friendliness, and their ability to be synthesized many different ways (electrochemical, chemical, sol−gel, hydrothermal, *etc.*).[11−13]

In terms of energy storage, manganese oxides have a long history as they were used in the first Leclanché alkaline battery cell developed in the 1860s.[14] Currently, they are being studied as cathode materials for lithium ion batteries[15−17] and as fast charging materials for supercapacitors.[18−20] In this latter application, they have underperformed as most research articles demonstrate capacitances of ≤470 F/g, which is far

* Address correspondence to slee@umd.edu.

Received for review September 27, 2012 and accepted January 17, 2013.

Published online January 17, 2013
10.1021/nn3056077

short of their theoretical capacitance of 1110 F/g.[21] It is thought that these meager numbers can be improved by nanosizing its structure as the energy storage mechanism is localized at the surface of the material.[22]

However, it must be kept in mind that these nanosized MnO_2 particles must be interconnected in some fashion in order to maintain their electrochemical activity. Therefore, by utilizing a hierarchical structure, one MnO_2 architectural dimension can provide a continuous interconnected substrate on which the smaller MnO_2 architecture dimension can be deposited. This could result in a synergic relationship between the two architectures.

Hierarchical MnO_2 nanostructures have been successfully synthesized previously. Fei *et al.* have created hollow MnO_2 microspheres and microcubes with nanometer scale shell thickness by reacting solutions of $KMnO_4$ with $MnCO_3$ microspheres and microcubes followed by dissolution of the $MnCO_3$.[10] Li *et al.* were able to create core−shell MnO_2 microspheres with spherically aligned MnO_2 nanorods on the surface by a one-step solution method utilizing a Ag catalyst.[23] Yu *et al.* created urchin-like clusters of MnO_2 nanorods by a hydrothermal method.[24] A great review containing other hierarchical MnO_2 nanostructures and additional recent advances in metal oxide architecture design was done by Jiang *et al.*[25] However, each of these methods is limited to manganese oxide materials, and they have limited control over the dimensions of the structures. Thus, it is highly desirable to develop a model electrochemical method to build high surface area hierarchical structures with various materials, aspect ratios, along with other architectural considerations in order to maximize each architecture's contribution to the whole structure.

We describe here a simple self-limiting electrochemical pathway of producing hierarchical MnO_2 nanostructures by exploiting the rich oxidation state chemistry of manganese oxide. This hierarchical material consists of template-synthesized nanowire arrays of MnO_2 conformally coated with nanofibrils of MnO_2. The template method provides great control over the parameters for each of the architectures including their diameter, length, and thickness. The adjustable length and diameter of the nanowires provide a continuous substrate for electron transfer onto which various amounts of the higher surface area nanofibrils are attached. This method does not require any use of binders or conductive additives as our electrodes consist of freestanding bare and hierarchical MnO_2 nanowires directly contacted to a gold current collector. This reduces any errors involved in the calculation of capacitance values that could be associated with double-layer capacitance from the conductive carbon or blockage of electrolyte from the polymeric binder.

The mechanism of formation for these nanofibrils is elucidated by electrochemical measurements, Raman spectroscopy, electron energy loss spectroscopy (EELS), and electron microscopy.

The MnO_2 hierarchical structures were then investigated at low scan rates (<10 mV/s) as supercapacitor materials in both an aqueous and organic (acetonitrile) solvent. The charge storage mechanism of the nanofibrils is shown to differ depending on the solvent used. These results indicate that the solvent chosen has a great effect on the charge storage mechanism and can be the major defining factor on whether the material obtains its theoretical capacitance.

Next, the hierarchical structure was tested at high scan rates in aqueous solution while varying parameters such as the length of the nanowires, the diameter of the nanowires, and the amount of nanofibrils deposited. These results indicate the following: (1) A shorter length can increase the specific capacitance but at the cost of the areal capacitance. (2) A smaller diameter nanowire increases the specific capacitance of the bare nanowires and that of the whole hierarchical structure but does not improve the supercapacitor performance of the nanofibrils. (3) The amount of nanofibrils deposited increases the specific capacitance of the hierarchical material; however, at excessive amounts, the nanofibrils become detrimental to the overall specific capacitance.

In addition, unlike synthesis methods for other hierarchical MnO_2 nanostructures, this electrochemical synthesis method can be easily applied to other MnO_2 systems and is shown here to produce additional hierarchical/heterogeneous $Ni(OH)_2/MnO_2$ and $Co(OH)_2/MnO_2$ nanofibril/nanowire arrays.

RESULTS AND DISCUSSION

Synthetic Mechanism of Hierarchical MnO_2 Nanowire/Nanofibril Arrays. Hierarchical MnO_2 nanowire/nanofibril arrays are synthesized by the following method. First, vertically aligned nanowire arrays of manganese oxide attached to gold are synthesized using a common anodic deposition process (Figure 1a).[26,27]

A nanofibril MnO_2 coating is then produced by the application of −0.85 V *vs* Ag/AgCl in a Mn^{2+} solution to the bare MnO_2 nanowire arrays which are then oxidized by a potential sweep to 1 V *vs* Ag/AgCl in a 1 M $LiClO_4$ electrolyte.

The proposed mechanism of formation for these hierarchical arrays is represented by Figure 1b and begins with the aforementioned electrochemical reduction of MnO_2 in a Mn^{2+} solution which is represented by "1" in Figure 1b. This results in two simultaneous reactions represented by the following reactions:

$$2MnO_2(s) + H_2O(l) + 2e^- \rightarrow Mn_2O_3(s) + 2OH^-(aq) \quad \textbf{(1a)}$$

$$Mn^{2+}(aq) + 2OH^-(aq) \rightarrow Mn(OH)_2(s) \quad \textbf{(1b)}$$

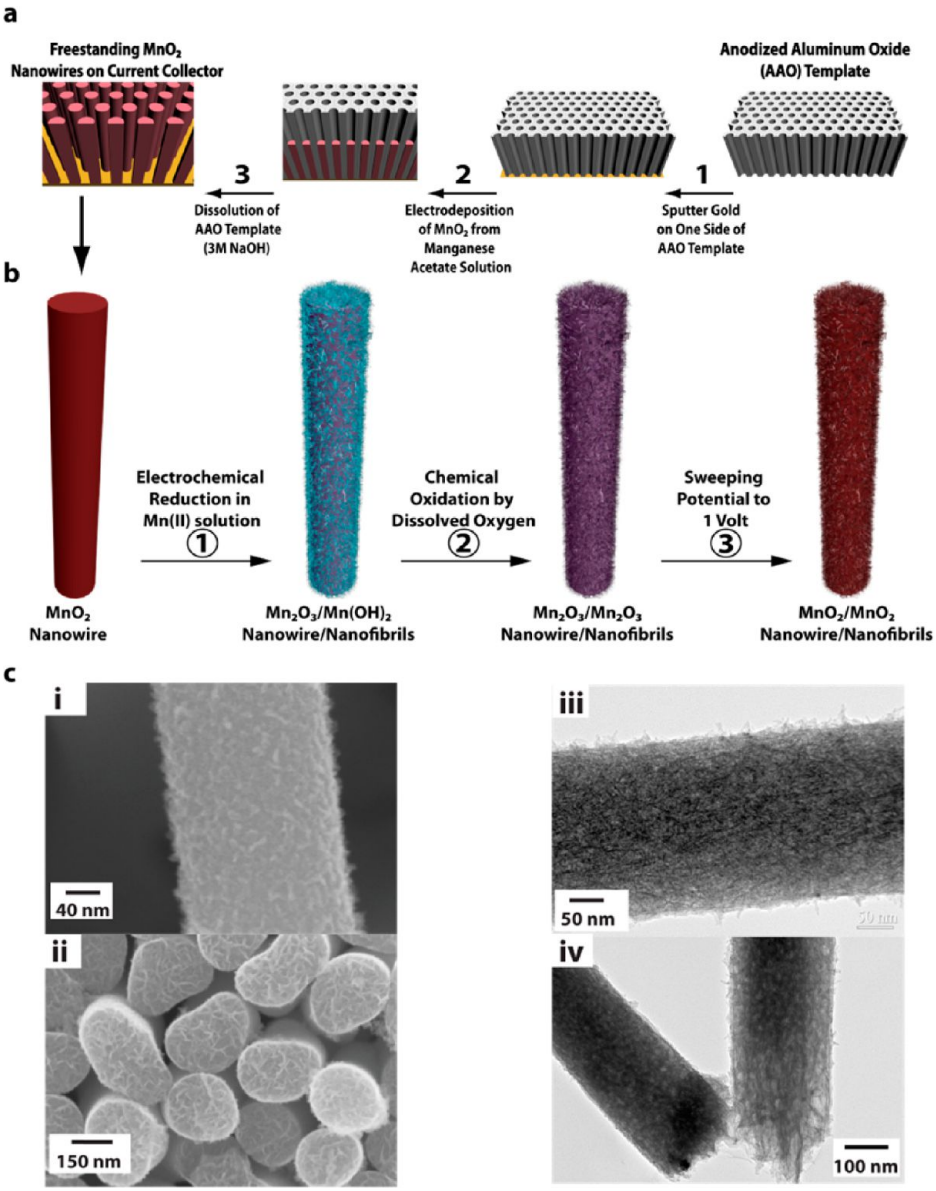

Figure 1. (a) Schematic diagram representing the electrochemical template synthesis of arrays of MnO_2 nanowires; (b) schematic diagram demonstrating the electrochemical synthesis of MnO_2 nanofibrils on MnO_2 nanowires; (c) SEM and TEM images of hierarchical MnO_2 nanowire/nanofibrils: (i) high magnification SEM image of nanofibrils on a single nanowire, (ii) SEM top-view of an array of MnO_2 nanofibril/nanowires, (iii) TEM image of the nanofibrils along the axis of the MnO_2 nanowire, and (iv) TEM image of the end structure of two nanofibril-coated nanowire.

Reaction 1a represents the reduction of the MnO_2 nanowires to Mn_2O_3, while reaction 1b represents the synthesis of $Mn(OH)_2$ nanofibril coating. The first reaction is a well-established mechanism found in alkaline batteries which releases hydroxide ions[28] that are needed for reaction 1b. The reduction potential used here was −0.85 V *vs* Ag/AgCl, which was chosen as a way to increase the reaction kinetics of the bulk OH^- production while avoiding the reduction of water. This is demonstrated by the linear sweep voltammetry found in Supporting Information Figure S1.

Reaction 1b is proposed based on manganese's Pourbaix diagram which shows that increasing the pH of a Mn^{2+} solution results in the formation of $Mn(OH)_2$.[29] In this case, the pH is only increased locally around the reducing MnO_2 nanowires, resulting in $Mn(OH)_2$ production localized at the surface of these nanowires.

Consequently, since reaction 1b relies on the production of hydroxide ions from reaction 1a, the amount of nanofibrils that can be produced is limited by the amount of MnO_2 available initially. Therefore, the production of the $Mn(OH)_2$ nanofibrils is self-limiting.

This is further supported by the following simple experiment: by controlling the amount of charged passed (750, 375, and 225 mC/cm^2) during the electrodeposition, different amounts of MnO_2 are synthesized in anodized aluminum oxide (AAO) templates and then directly reduced in the same Mn^{2+} electrodeposition

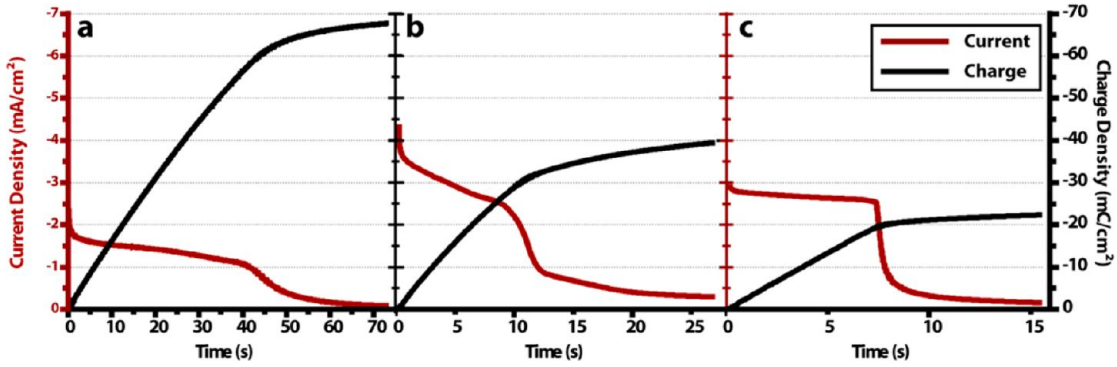

Figure 2. Curves for current (red) and charge (black) density *versus* time during the electrochemical reduction of MnO_2 in an AAO template where a, b, and c correspond to the initial electrodeposited MnO_2 amounts of 750, 375, and 225 mC/cm^2, respectively.

solution. The curves for current and charge density *versus* time during the reduction are represented by Figure 2 where a, b, and c correspond to the initial electrodeposited MnO_2 amounts of 750, 375, and 225 mC/cm^2, respectively. The current dramatically falls to near zero when the charge reaches or approaches half the charge density of the electrodeposition (a, 350; b, 200; and c, 120 mC/cm^2).

This correlates well with the assumption that, during the electrodeposition, the manganese species oxidizes from Mn^{2+} to Mn^{4+}, while during the reduction, the Mn^{4+} reduces to Mn^{3+}. In other words, only half of the charge passed during electrochemical deposition can be used during the reduction process. This means that the amount of hydroxide that can be formed by reaction 1a is limited to the amount of MnO_2 (Mn^{4+}) that is initially electrodeposited. Next, the manganese hydroxide nanofibrils formed in 1b are highly unstable and react within minutes with dissolved oxygen to form Mn_2O_3 which corresponds to process "2" in Figure 1b. This is represented by the following reaction.[30]

$$6Mn(OH)_2(s) + O_2(g) + 2OH^- \rightarrow 3Mn_2O_3(s) + 7H_2O(l) \quad (2)$$

The final step in the formation of the MnO_2 nanowire/nanofibril arrays, represented by "3" in Figure 1b, is the total oxidation of the Mn_2O_3 nanowires and nanofibrils to MnO_2 during the first potential sweep of the electrode to 1 V *vs* Ag/AgCl. This is just the reverse of reaction 1a, represented by the following reaction:

$$Mn_2O_3(s) + 3H_2O(l) \rightarrow 2MnO_2(s) + 2H_3O^+(aq) + 2e^- \quad (3)$$

The resulting MnO_2 nanowire/nanofibril structures can be seen in the SEM and TEM images in Figure 1c. The structures consist of MnO_2 nanowires coated with a conformal layer of MnO_2 nanofibrils. Thus, the MnO_2 nanowires provide a high surface area substrate on which the smaller nanofibrils precipitate. The thickness of the nanofibril layer is estimated to be between 5 and 10 nm from SEM imaging; however, due to blurring effects at these high magnifications, there is a large error in this measurement.

Characterization of the MnO_2 Nanofibril/Nanowire Structure with Raman and EELS. Since our material displays small crystal sizes without any long-range order, analysis by X-ray diffraction was not possible as the results showed no clear diffraction peaks. Thus Raman spectroscopy was chosen here to analyze the formation mechanism of our MnO_x material due to its ability to show average crystal structure over a large area. Raman spectrum 3a represents MnO_2 nanowires as initially electrodeposited. The peaks seen at 573 and 649 cm^{-1} correspond well with literature values for the δ phase MnO_2 Raman spectrum[31,32] as well as our own Raman analysis of manganese standards found in Supporting Information Figure S2. This phase consists of layered sheets of MnO_6 octahedra. Accordingly, the peak at ≈575 cm^{-1} has been attributed to Mn−O stretching in the basal plane of the MnO_6 sheet, while the peak at ≈650 cm^{-1} has been attributed to MnO_6 symmetric stretching vibrations.[31]

Figure 3b,d represents MnO_2 nanowires reduced in Mn^{2+} and Li^+, respectively. MnO_2 is reduced in Li^+ here to better illustrate the oxidation state of the underlying nanowires as no MnO_x nanofibrils will be formed during this reaction as was found in Supporting Information Figure S3, where MnO_2 nanowires embedded in AAO were reduced in manganese ion (Figure S3a) and manganese ion-free (Figure S3b) solutions and production of $Mn(OH)_2$ was only seen in the former. Thus, the material reduced in Li^+ has peaks at 590 and 623 cm^{-1}, which suggests that the MnO_2 nanowire is reduced to Mn_2O_3,[33] while the MnO_2 reduced in Mn^{2+} showcases a broad peak at 608 cm^{-1}.

This reduction of the MnO_2 nanowire to Mn_2O_3 process is further examined by electron energy loss spectroscopy (EELS), as shown in Figure 4. First, the EELS spectra of three standard samples purchased from Sigma-Aldrich consisting of MnO_2, Mn_2O_3, and

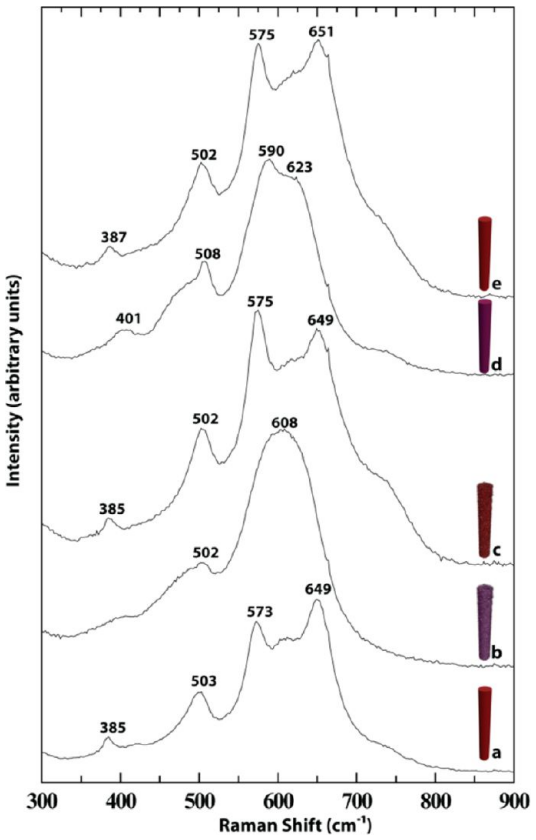

Figure 3. Raman spectroscopy of (a) electrodeposited MnO_2; (b) MnO_2 reduced in a Mn^{2+} solution; (c) "b" after sweeping the potential to 1 V *vs* Ag/AgCl; (d) MnO_2 reduced in Li^+ solution; (e) after sweeping the potential of "d" to 1 V *vs* Ag/AgCl.

Mn_3O_4 were obtained. These spectra show the characteristic O K- and Mn $L_{2,3}$-edges. The different edge details for each of the standards for the O K-edge can be used as a fingerprint to obtain valence information for unknown samples.[34,35]

Figure 4b is the dark-field TEM image of a MnO_2 nanowire partially reduced in Mn^{2+} before release from the AAO template. In this case, only the end of the nanowire which is exposed to the Mn^{2+} solution is reacted (an SEM image of this can be found in Supporting Information Figure S3a). This in-template reduction method was used to promote a sharp interface between the MnO_2 nanowire and the reduced MnO_x that is formed during the reduction stage of the hierarchical synthesis. As can be seen in Figure 4b, there is a sharp visual contrast between the MnO_2 nanowire and the reduced MnO_x part of the nanowire.

Points along the axis of this nanowire were probed using EELS, as can be seen in Figure 4c. These points progress from the MnO_2 portion of the nanowire (i) to the edge where the MnO_2 is reduced (vi). As exhibited from the data, the shape of the O K-edge transforms from that characteristic of MnO_2 to that characteristic of Mn_2O_3. Thus the EELS data show that the MnO_2 nanowire is converted to Mn_2O_3 during the reduction process. This EELS data correlate well with our assumption that the MnO_2 nanowire reduces to Mn_2O_3 upon application of a negative potential.

A closer examination of the Raman data in Figure 3ii,iv reveals that the peak at 608 cm^{-1} for the Mn^{2+} reduced MnO_2 is a possible convolution of the two peaks in the spectrum of the Li^+ reduced MnO_2. This convolution may be caused by the smaller particle size and reduced crystallinity of the nanofibrils. In fact, in our own Raman analysis of a Mn_2O_3 standard, we saw this same convoluted peak (see Supporting Information Figure S2). This suggests that the nanofibrils are Mn_2O_3, which correlates well with our assumption of $Mn(OH)_2$ nanofibril formation followed by a rapid oxidation to Mn_2O_3.

Finally, the materials represented by Raman spectrum in Figure 3b,d are potentially swept to a voltage of 1.0 V *vs* Ag/AgCl. This represents a typical first charge of a supercapacitor electrode. The spectra represented by Figure 3c,e demonstrate that both materials are oxidized to MnO_2 by evaluating their characteristic MnO_2 Raman peaks of ≈575 and ≈650 cm^{-1}.

X-ray photoelectron spectroscopy (XPS) studies were also done to try to correlate this Raman and EELS data; however, we found the results inconclusive as the peak separation of the Mn 3s multiplet only varied between 5.2 and 5.4 eV, indicating a valence state of 3^+ for Mn[36] under all electrochemical states. This can be attributed to the high surface area of our material, which is most likely to contain MnOOH due to the synthesis in an aqueous solvent. Ion milling of our samples for this XPS work was initially suggested to show the true valence state below the surface; however, oxygen is sputtered more preferentially than manganese, which would show an artificially lower valence state in the bulk resulting in less than true valence state measurements. Nonetheless, these Raman and EELS results support our proposed mechanism of formation for these hierarchical MnO_2 nanowire/nanofibril arrays.

EDS and XPS from Applications to Other Systems. As a final support of our synthesis mechanism, it was demonstrated in other systems. Herein, MnO_2 nanowire arrays are reduced in Ni^{2+} and Co^{2+} solutions. Figure 5a (MnO_2 reduced in Ni^{2+}) and 5c (MnO_2 reduced in Co^{2+}) show the energy-dispersive X-ray spectroscopy (EDS) line scans for these hierarchical heterogeneous structures. Both graphs illustrate a MnO_2 nanowire core with an oxide of nickel or cobalt nanofibril shell, respectively.

The oxidation state of these nanofibril shells is probed by XPS. The results show that the main peak found in Figure 5b (MnO_2 reduced in Ni^{2+}) for the Ni $2p_{3/2}$ multiplet is positioned at 855.3 eV, which corresponds well with literature values for $Ni(OH)_2$.[37] The fitted components found in Figure 5d (MnO_2 reduced in Co^{2+}) for the Co $2p_{3/2}$ multiplet (790.8, 786.1, 781.9, and 780.4 eV) match well with the calibrated (C1s = 284.8 eV)

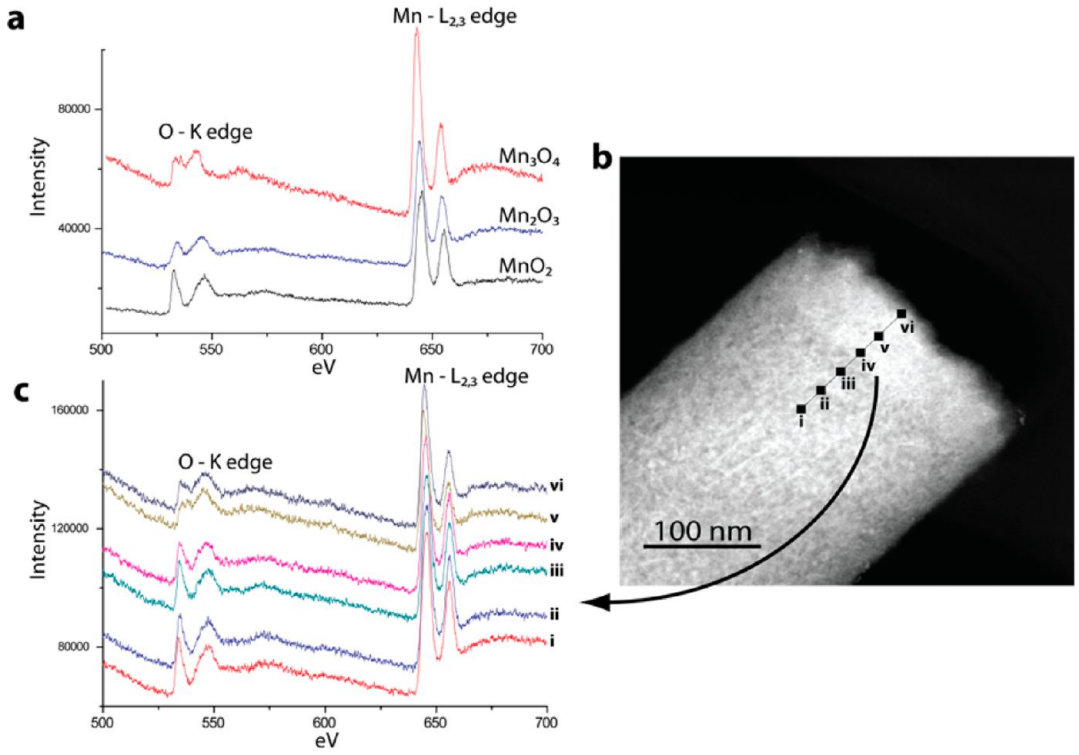

Figure 4. (a) Electron energy loss spectroscopy (EELS) spectra of standards of MnO_2, Mn_2O_3, and Mn_3O_4; (b) dark-field image of end structure of MnO_2 nanowire reduced in Mn^{2+} in an AAO template; (c) EELS spectra of points i–vi found in "b" indicating phase of MnO_x along the axis of the nanowire.

literature values found for $Co(OH)_2$ (790.5, 786.1, 782.3, and 780.5 eV).[38]

This formation of hydroxides from metal solutions during the reduction of MnO_2 correlates well with our assumption that the reduction of MnO_2 releases OH^- ions that combine with the metal ions in solution. These metal hydroxides are then shown to precipitate out of solution as nanofibrils. This also demonstrates the ability of this method to be easily applied to other materials.

Supercapacitor Application. *Low Power Investigation of the Charge Storage Mechanism.* For investigation of the supercapacitor charge storage mechanism of this hierarchical structure, the nanomaterial was studied in the low power realm (scan rate = <10 mV/s). The material was tested in both aqueous and organic (acetonitrile) solvent with lithium perchlorate as the inorganic salt. The voltage window was kept between 0 and 1 V *vs* Ag/AgCl for both electrolytes to directly compare the charge storage properties in the different solvents.

Figure 6 shows that the material in both solvents shows an increase in specific capacitance for the whole hierarchical material (Hier) upon addition of the nanofibrils when compared to the bare nanowire (Bare) counterparts (from 289 to 345 F/g for the aqueous solvent and from 324 to 387 F/g for the organic solvent) at a 0.5 mV/s scan rate. Note, all masses were attained from inductively coupled plasma-atomic emission spectroscopy (ICP-AES) elemental analysis (see Supporting Information Figure S4).

The improvement in gravimetric capacitance may seem minor, but the improvement in areal capacitance is more dramatic. In aqueous electrolyte, the nanofibrils improve areal capacitance by 42.5% (from 128 to 181 mF/cm^2). In organic electrolyte, the improvement is similar, with areal capacitances increasing 42.0%, from 143 to 203 mF/cm^2. These total capacitance increases of 42.5 and 42.0% for the aqueous and organic solvent, respectively, are achieved with only a total mass increase of 19.3%. (Note, the planar area of the working electrode was maintained at 0.2 cm^2 for all materials.)

Owing to this, we can obtain the specific capacitance associated with the nanofibrils if we divide the difference in total capacitance by the difference in the mass between the Hier and Bare arrays. The outcome of this calculation is a specific capacitance of 628 and 718 F/g attributed to the nanofibrils for the aqueous and organic solvents, respectively.

This large specific capacitance is thought to be due to both the ultrahigh surface area and small dimensions of the nanofibrils; however, due to the low mass loading of our material, reliable BET measurements were not possible. The ultrahigh surface area can increase capacitive adsorption and double-layer performance, and the small dimensions can increase ion access points and shorten diffusion distances for any

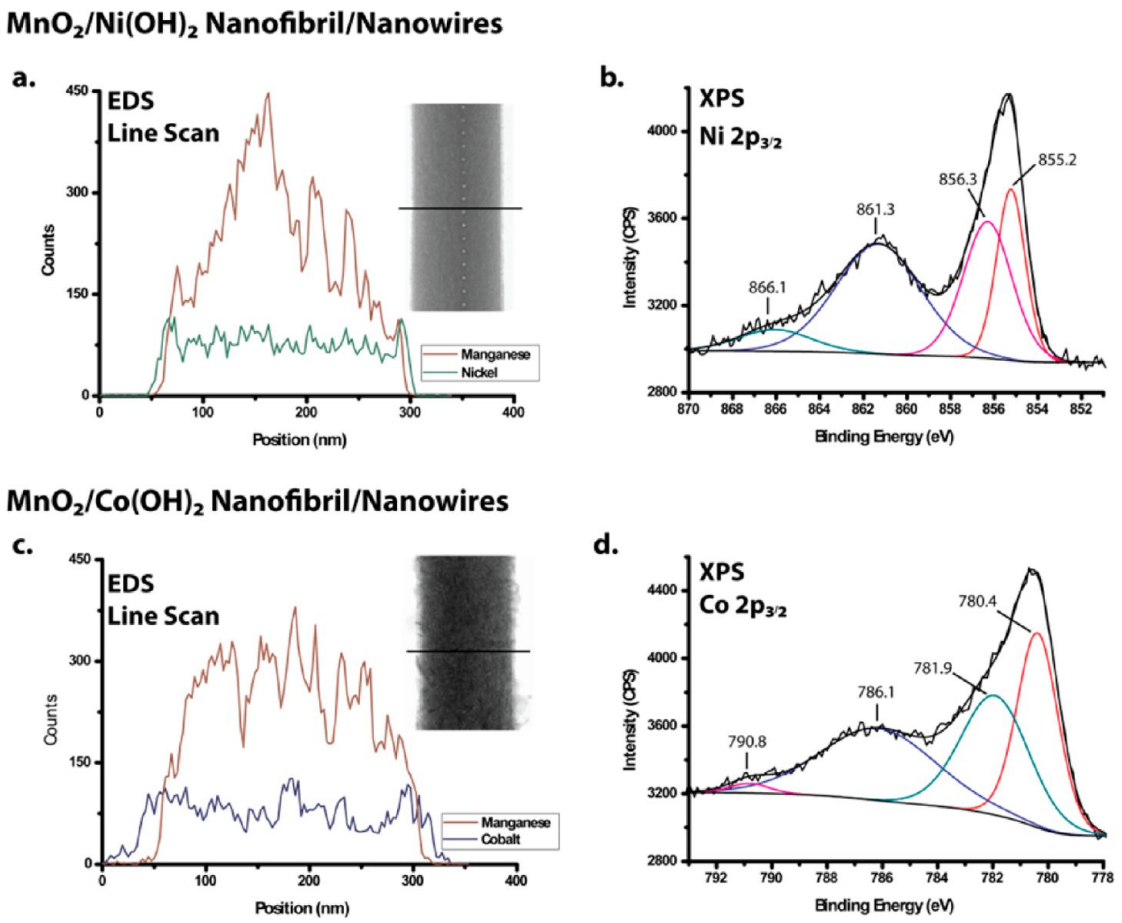

Figure 5. Energy-dispersive X-ray spectroscopy (EDS) line scans for MnO_2 nanowires reduced in (a) Ni^{2+} and (c) Co^{2+} and the XPS spectrum of the $2p_{3/2}$ multiplet for (b) Ni and (d) Co from these structures.

insertion processes. Although these values are appealing, it is interesting to see how differently this extra charge is stored whether it be more by capacitive elements or insertion elements in each respective electrolyte.

Two different methods were used to investigate the charge storage mechanisms in the hierarchical structure. First, we use a method derived from Conway *et al.*[39] by Dunn *et al.*[40] and used recently by Penner *et al.*[21] to quantitatively separate the contribution of the capacitive elements of the charge storage from the diffusion-controlled insertion processes. By examining the scan rate dependence of the current, one can estimate that the current at each voltage is the sum of both contributions to the capacitance using the following formula:

$$i(V) = k_1 v + k_2 v^{1/2} \quad (4)$$

where $i(V)$ is the current at a given voltage, k_1 and k_2 are constants, and v is the scan rate. In this equation, $k_1 v$ represents the capacitive elements or elements where di/dv is constant while $k_2 v^{1/2}$ represents diffusion-controlled bulk reactions where $di/dv^{1/2}$ is constant. If we divide both sides of this equation with the square root of the scan rate, then we get the following equation:

$$i(V)/v^{1/2} = k_1 v^{1/2} + k_2 \quad (5)$$

Therefore, if we plot the $i/v^{1/2}$ at a given potential *versus* $v^{1/2}$, we should obtain a line with the slope equaling constant k_1 and the *y*-intercept equaling k_2, thus giving us a quantitative way of separating the capacitive elements, $k_1 v$, from the bulk reactions, $k_2 v^{1/2}$, at each given voltage.

If we look at Figure 6 again, we can see the results of using this method. Here, the hashed areas are attributed to a capacitive charge storage reaction. Figure 7 shows these results at different scan rates (0.5 and 10 mV/s) in terms of areal capacitance. These results indicate that the Hier material's increase in capacitance from the aqueous solvent comes mainly from an increase in capacitive charge storage (118.4 to 170.6 mF/cm^2 at the 0.5 mV/s scan rate), which is mainly due to the high surface area of the nanofibrils. However, the increase in capacitance from the organic solvent comes from an increase in cation insertion (7.0 to 66.7 mF/cm^2 at the 0.5 mV/s scan rate), which results from the short diffusion distance of the nanofibrils.

Another method developed by Trasatti to separate capacitive elements from insertion processes is used

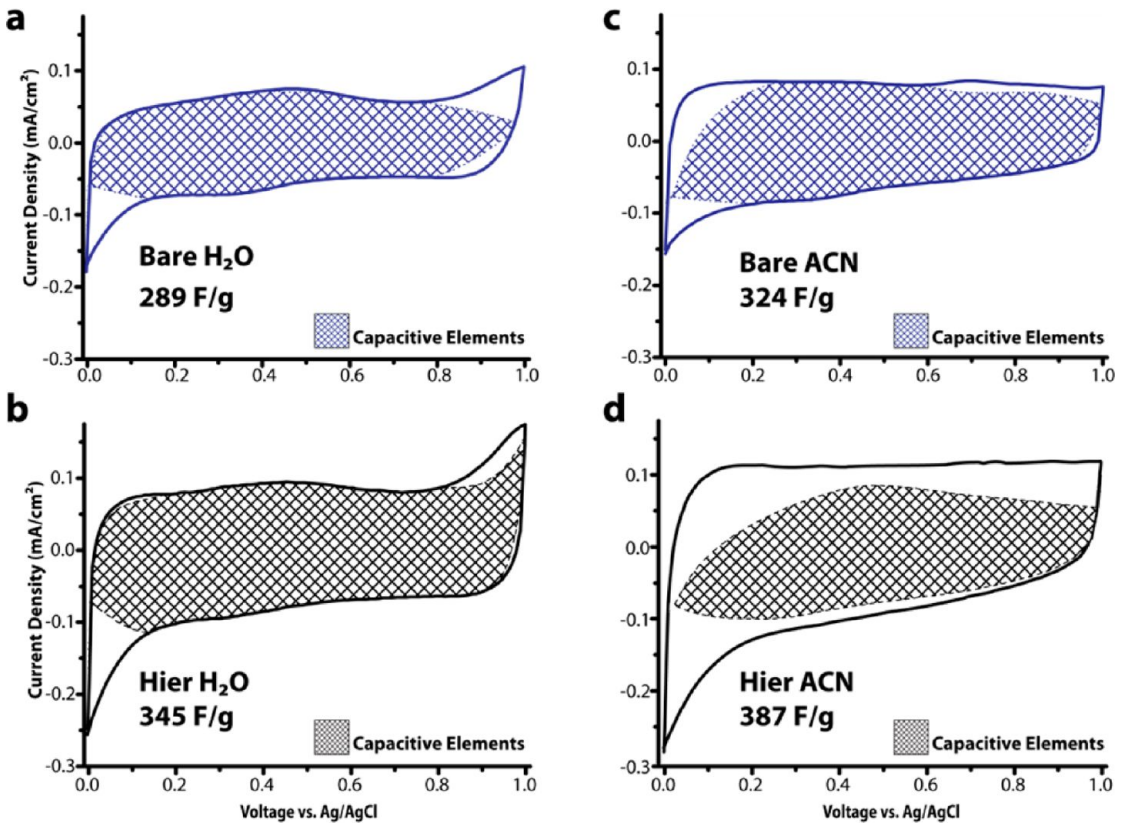

Figure 6. Cyclic voltammetry at a 0.5 mV/s scan rate with the hashed area representing the part of the curve that contains capacitive elements of a (a) bare MnO_2 nanowire array and (b) hierarchical MnO_2 nanowire cycled in an aqueous 1 M $LiClO_4$ solution and a (c) bare MnO_2 nanowire array and (d) hierarchical MnO_2 nanowire cycled in an organic acetonitrile 1 M $LiClO_4$ solution.

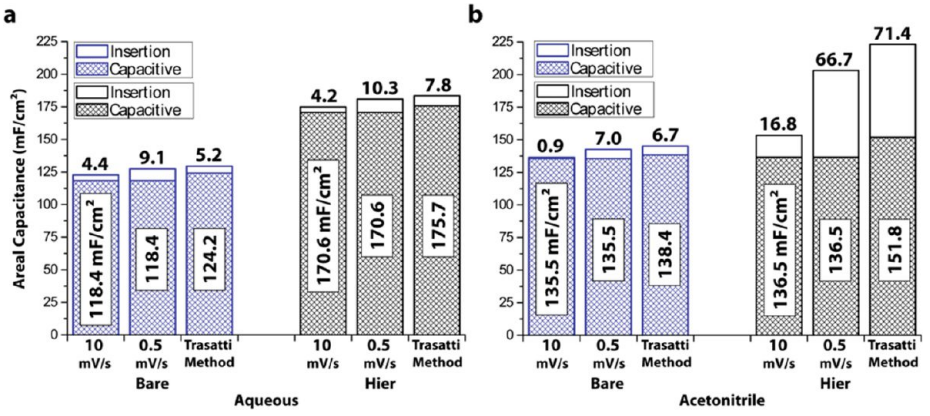

Figure 7. Bar graph of bare (blue) and hierarchical (black) MnO_2 nanowire arrays' areal capacitance *versus* scan rate with the hashed areas representing the capacitance attributed to only capacitive elements derived from Dunn's method and the maximum capacitances derived from Trasatti's method in different solvents: (a) aqueous and (b) acetonitrile.

here.[41] Again a scan rate series is performed, but this time it is used to project what the capacitance will be at the scan rates of 0 and infinity. The capacitance at 0 mV/s will demonstrate the total capacitance (C_t) if we allowed sufficient time for every reaction to take place, while the capacitance at an infinite scan rate will tell us only the charge stored at the surface (C_s). The difference between the total capacitance and surface capacitance ($C_t - C_s$) will give us the capacitance associated with the insertion processes (C_i).

First, we obtain the maximum capacitance associated with the surface charges by plotting the capacitance, C, *versus* the inverse square root of the scan rate, $\upsilon^{-1/2}$, for both the bare and hierarchical structure, as seen in Figure 8a,c for the aqueous and organic solvents, respectively. (All of the values used in Figure 8 and the slopes and intercepts obtained in Figure 8 can be found in the Supporting Information Table 1.) Here, we assume there is semi-infinite linear diffusion, so we expect a linear correlation between C and $\upsilon^{-1/2}$.

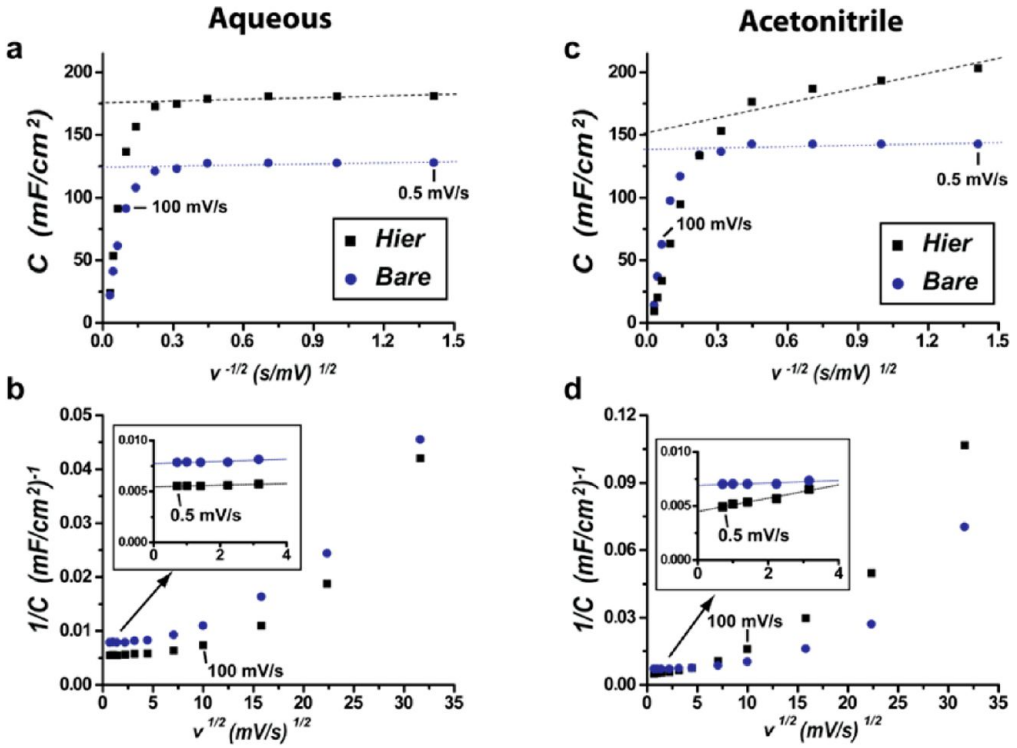

Figure 8. (a,c) Areal capacitance *versus* inverse square root of scan rate for bare (blue circles) and hierarchical (black squares) MnO_2 nanowire arrays cycled in (a) aqueous and (c) acetonitrile solvent electrolytes. (b,d) Inverse areal capacitance *versus* square root of scan rate for bare (blue circles) and hierarchical (black squares) MnO_2 nanowire arrays cycled in (b) aqueous and (d) acetonitrile solvent electrolytes with the inset representing the linear aspect of these points at low scan rates.

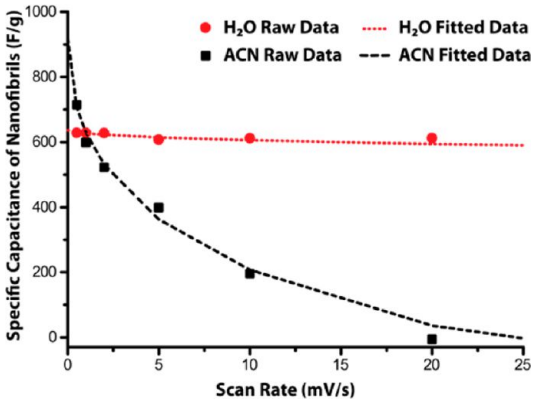

Figure 9. Specific capacitance attributed to the nanofibrils at various scan rates for the hierarchical MnO_2 material cycled in aqueous (red circles) and acetonitrile (black squares) solvents with the dashed lines representing the fitted curve based on Trasatti's method.

However, Figure 8a,c deviates from linearity at high scan rates. This is caused by ohmic drops and irreversible redox transitions owing to the resistance of MnO_2.[42] Therefore, we fit the curve only at low scan rates (0.5 to 10 mV/s) where the points are close to linear. Using this curve, we can obtain $v^{-1/2} = 0$, which represents the maximum surface capacitance of the material. These results can be found in the hashed areas of the bar graphs labeled "Trasatti Method" in Figure 7.

Furthermore, we plotted the inverse of the capacitance *versus* the square root of the scan rate. This can be observed in Figure 8b,c for the aqueous and acetonitrile solvent. Again, we extrapolate the curve at low scan rates, this time to $v^{1/2} = 0$. Here, we obtain the total maximum capacitance. These values can be seen in Figure 7 along with the results from the Dunn method for the scan rates of 0.5 and 10 mV/s. In comparison, both the Dunn method and Trasatti method show similar quantitative results with a better correlation between the methods at the smaller scan rates.

If we further utilize Trasatti's method to obtain the specific capacitance only attributed to the nanofibrils, then we can extrapolate the maximum specific capacitance of the nanofibrils at a 0 scan rate. Thus, the specific capacitance of the nanofibrils at a given scan rate, SC_{nfs}, can be obtained using the following equation:

$$SC_{nfs} = \frac{\left(\frac{1}{a_{hier}v^{1/2} + b_{hier}}\right) - \left(\frac{1}{a_{bare}v^{1/2} + b_{bare}}\right)}{m_{hier} - m_{bare}} \times A \quad (6)$$

where a represents the slope and b represents the y-intercept of the fitted lines found in Figure 8b,d for the aqueous and organic solvents, respectively; v represents the scan rate, A represents the area of the electrode (0.2 cm^2), and m represents the mass of the bare and hierarchical nanowire arrays.

Figure 9 shows the raw data obtained from the scan rate series and the fitted data utilizing Trasatti's method for both the aqueous and organic solvents. The nanofibrils cycled in aqueous solution appear to have

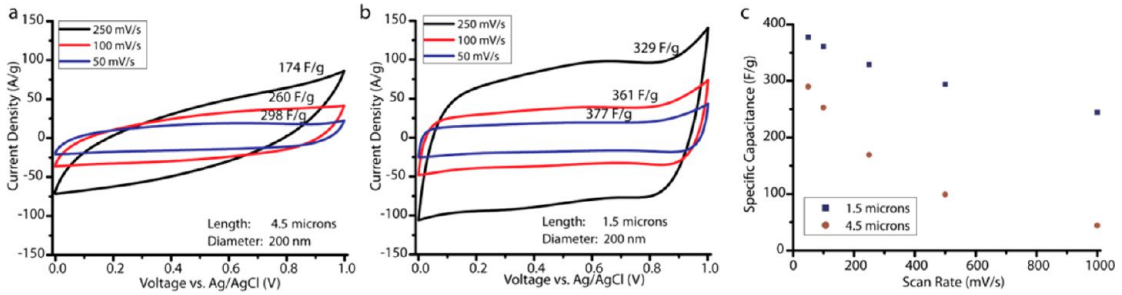

Figure 10. Cyclic voltammetry curves in aqueous 1 M $LiClO_4$ from 50 to 250 mV/s scan rates for the (a) 4.5 μm and (b) 1.5 μm long hierarchical nanowire arrays and the power capability from 50 to 1000 mV/s scan rate for the 4.5 and 1.5 μm length hierarchical nanowires.

nearly reached their maximum capacitance of 637 F/g at a 0.5 mV/s scan rate, while the nanofibrils cycled in the acetonitrile solvent appear to need exceedingly slow scan rates to come close to their maximum capacitance of 919 F/g.

This is a very interesting result as it shows that, in the acetonitrile solvent, the MnO_2 nanofibrils can reach close to their theoretical maximum capacitance; however, in the aqueous solvent, these same MnO_2 nanofibrils reach a maximum capacitance far below their theoretical value. This correlates well with our projection that the nanofibrils in aqueous solution only contribute fast surface capacitance, thus they do not need exceedingly slow scan rates to reach their maximum specific capacitance. In organic solution, the nanofibrils utilize slow cation diffusion which does need very slow scan rates to fully make use of the material. Accordingly, one would expect that, at a scan rate of zero, the material would exhibit the full theoretical capacitance of 1110 F/g based on one-electron transfer; however, due to manganese oxide's low intrinsic conductivity, the data used to create Trasatti's curve in Figure 9 could be skewed to create a lower maximum specific capacitance.

Qualitatively, we can see that with the Trasatti method the nanofibrils have mainly a capacitive charge storage element in aqueous solution and mainly an insertion charge storage element in the organic electrolyte. This different charge storage mechanism in the different solvents is believed to be due to the proton adsorption behavior in water which mitigates the lithium insertion mechanism. In fact, in literature, it has been shown that the cation does not play a major role in the charge storage mechanism in aqueous solutions.[43] Currently, we are investigating these different charge storage mechanisms using ICP-AES. However, it is interesting to note that, regardless of the predominant charge storage mechanism, the nanofibril structure produces an advantage for overall performance.

High Power Investigation for Practical Applications. It was shown in the previous section that, at low scan rates, the charge storage mechanism of the material can be obtained. However, for real supercapacitor applications, the material must show superior high power capabilities. For investigation of the practical supercapacitor properties of this hierarchical structure, the nanomaterial was studied at high power rates (>50 mV/s). For this high power testing, the material was only tested in an aqueous solvent due to its intrinsically high ionic conductivity and low environmental impact.[44]

Figure 10a shows the cyclic voltammetry curves of the hierarchical material at high scan rates, 50, 100, and 250 mV/s. Although the shape of the curve and the capacitance of the material (260 F/g) at 100 mV/s are promising for future applications, it is shown here that, at the higher scan of 250 mV/s, the shape of the CV curve begins to have a sloping behavior and the capacitance drops dramatically.

Since MnO_2 is known as a poor electron conductor, the 4.5 μm long nanowires (aspect ratio = 22.5) would seem to be exceedingly long. Therefore, shorter lengths of $\approx$1.5 μm of hierarchical nanowires (aspect ratio = 7.5) were produced by reducing the charge passed by a third during the synthesis of the nanowires. The synthesis of the nanofibril layer was also cut by a third. Figure 10b indicates that these shorter hierarchical nanowires are able to maintain their CV shape at the higher scan rates. The rate capability comparison of these nanowires is further shown in Figure 10c.

Another benefit of the shorter nanowires is the increase in the specific capacitance (from 298 to 377 F/g at 50 mV/s). However, it should be noted that, although the gravimetric capacitance values increase with the shorter nanowires, the areal capacitance values decrease (from 156.5 to 66.0 mF/cm^2). Therefore, for future electrochemical energy storage, the benefits of higher gravimetric capacitance should be weighed against any losses in the areal capacitance.

Another aspect for this hierarchical material that can be varied is the amount of charge passed during the synthesis of the MnO_2 nanofibrils. Figure 11a shows the specific capacitance *versus* charge passed during the synthesis of the MnO_2 nanofibrils. The black squares in Figure 11a represent the specific capacitance associated with the whole hierarchical structure, while the red squares represent the specific capacitance

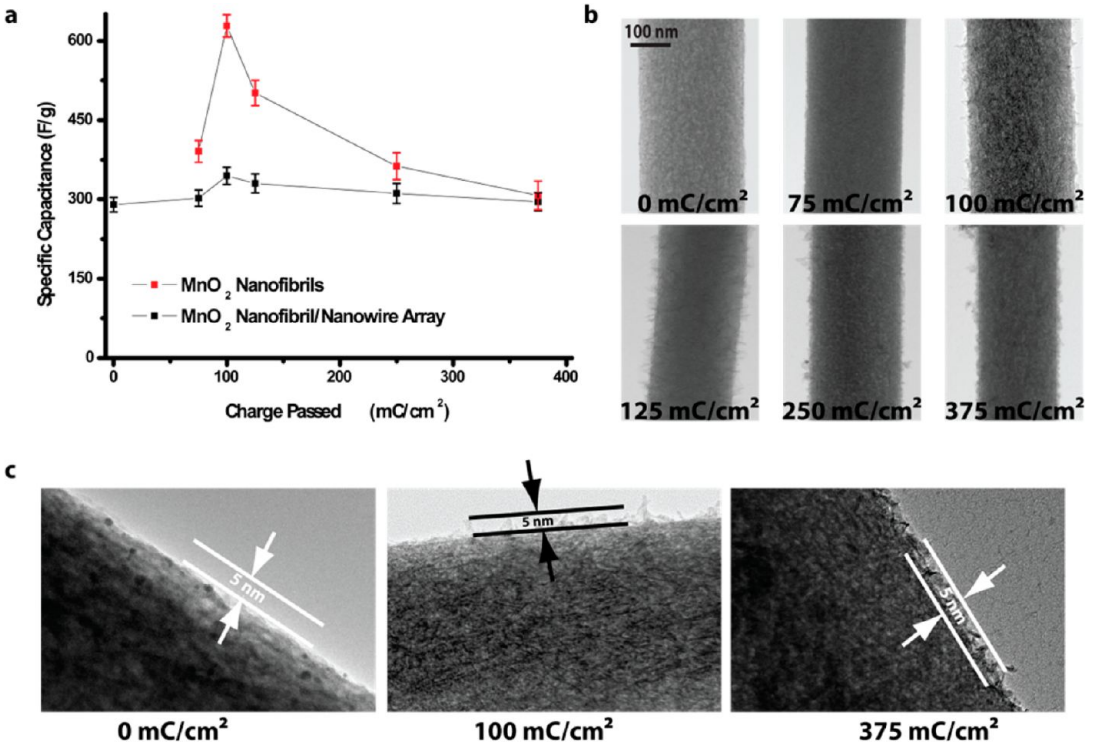

Figure 11. (a) Specific capacitance (50 mV/s) of the whole hierarchical structure and that attributed to the nanofibrils during different nanofibril loading amounts controlled by the amount of charged passed during the synthesis of these nanofibrils and (b) TEM images of these nanowires at the different stages along the graph in (a). (c) Magnified TEM images showing the thickness of the nanofibril layer as charge density is increased.

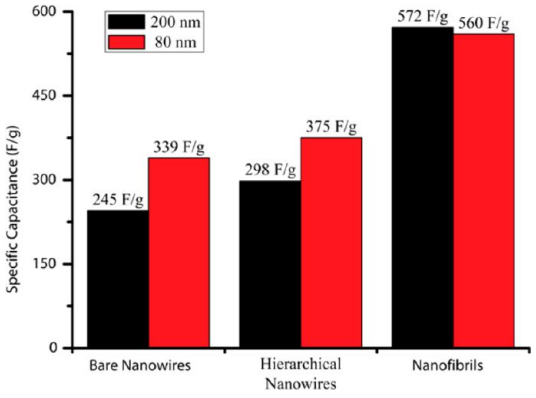

Figure 12. Specific capacitance (50 mV/s) comparison between 80 and 200 nm diameter nanowires showing the contribution from the individual architectures.

only associated with the MnO_2 nanofibrils. Figure 11b,c shows the TEM images at different loading amounts for the MnO_2 nanofibrils, with the upper left image in Figure 11b representing a smooth bare MnO_2 nanowire and the bottom right image representing a fully nanofibril-coated nanowire.

As demonstrated in the graphs, the specific capacitance for both the hierarchical structure and the nanofibrils reaches a peak at a total charge passed of 100 mC/cm^2 for the hierarchical MnO_2 material. An explanation for this peak shaped plot is that at lower charge densities, the nanofibrils produced from the fast effusion of the hydroxide ions from eq 1a are too frail and are not in good electrical contact with the MnO_2 nanowires and so are electrochemically inactive. At higher charge densities, the nanofibril material is in good electrical contact; however, as the amount of charge passed increases, the amount of coverage by the nanofibril layer ultimately reduces the access of the electrolyte to the nanowire. This reduces the specific capacitances associated with the MnO_2 nanofibrils to a number that is smaller than that associated with the pure MnO_2 nanowires.

Finally, the diameter of the nanowires was adjusted using AAO templates with 80 nm diameter pores during the synthesis process. As the charge storage mechanism is thought to be a near surface reaction, it is assumed that the smaller nanowires will reduce the amount of inactive MnO_2 resulting in larger specific capacitances. Figure 12 shows the comparison of the specific capacitance (50 mV/s) of the different diameter hierarchical nanowires. The results indicate that indeed the overall specific capacitance of the hierarchical nanowires increased when the diameter is decreased from 200 to 80 nm (298 and 339 F/g, respectively); however, it is noted that the specific capacitance associated with the nanofibrils is not greatly affected (572 F/g for 200 nm and 560 F/g for 80 nm). This is attributed to the fact that the amount of nanofibrils produced is not affected by the diameter of the nanowires.

Next, we show the cycle life of the hierarchical structure. Figure 13 shows the cycle ability of the 4.5 μm

long 200 nm diameter hierarchical array over 1000 cycles at a 50 mV/s scan rate. The material maintains 85.2% (254 F/g) of its specific capacitance after 1000 cycles, which is still better than the initial bare specific capacitance at this scan rate (245 F/g). Most of this capacitance loss occurs within the first 100 cycles and correlates well with the Coulombic efficiency during these initial cycles. It is thought that this may be due to some residual Mn_2O_3 to MnO_2 conversion associated with eq 3. After the initial cycle degradation, the material sees only a small drop in specific capacitance from 257 to 254 F/g for the remaining 900 cycles.

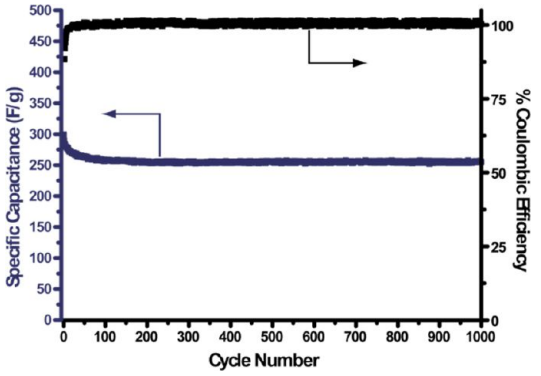

Figure 13. Cycle ability including specific capacitance (50 mV/s) and Coulombic efficiency of the hierarchical structure over 1000 cycles in 1 M $LiClO_4$ in water.

Finally, in order to compare our results with other hierarchical MnO_2 nanomaterials, we have included the tabulated information in Table 1. This table shows that, although our material may not have the highest capacitance, highest loading capability, or other superlatives, it does offer a controllable structure without the affects of binders and additives to gain scientific insight into the desired aspects of hierarchical MnO_2 nanomaterials.

CONCLUSION

A controllable hierarchical MnO_2 nanofibril/nanowire array was successfully synthesized. The structure consists of a conformal layer of MnO_2 nanofibrils evenly distributed on the surface of the MnO_2 nanowires. The synthesis of the MnO_2 nanofibril layer was done by a simple electrochemical conversion of the MnO_2 nanowires to Mn_2O_3 in a Mn^{2+} solution. Due to the hydroxide formation during this conversion, a $Mn(OH)_2$ nanofibril layer was formed at the surface of these nanowires, which quickly oxidized to Mn_2O_3. Subsequently, oxidation of both the Mn_2O_3 nanowires and Mn_2O_3 nanofibrils resulted in the formation of the hierarchical MnO_2 nanofibril/nanowire material. This structure was characterized by Raman, EELS, ICP-AES, electrochemical measurements, and electron microscopy.

At slow scan rates, this hierarchical nanowire structure showed an enhanced supercapacitor performance when compared to its bare nanowire counterpart in both

TABLE 1. Literature Survey of Hierarchical MnO_2 Supercapacitors

description	specific capacitance at low and high power	cycle retention rate	mass loading	synthesis method	binder and additives	control of structure
hollow urchin-like MnO_2 nanospheres[45]	167 F/g (2.5 mA) 124 F/g (10 mA)	89% after 350 cycles	≈10 mg (calcd)	hydrothermal	yes	some morphological control
hollow MnO_2 nanospheres[46]	299 F/g (5 mV/s) no high power testing shown	97.6% after 1000 cycles	≈7 mg (calcd)	SiO_2 nanosphere as sacrificial template	yes	none shown
3D porous birnessite-MnO_2[47]	194 F/g (0.1 A/g)	95% after 1000 cycles	≈11 mg (calcd)	hydrothermal using thermally reduced graphene oxide as template	yes	none shown
MnO_2 coated on Mn_3O_4 decorated MnOOH nanorods[48]	470 F/g (25 mV/s) 360 F/g (500 mV/s)	95.7% after 10000 cycles	≈50 μg/cm^2 (calcd)	pulsed electrochemical deposition	no	none shown
MnO_2 nanorods assembled into spheres[49]	356 F/g (2 A/g) 184 F/g (10 A/g)	"no degradation" after 2000 cycles	≈0.5 mg (calcd)	precipitation reaction of Mn^{2+} with Mn^{4+} in the presence of P123 micelles	yes	none shown
assembled MnO_2 nanowire flowers[50]	407 F/g (10 mV/s) 258 F/g (100 mV/s)	>90% after 400 cycles (dependent on charge rate)	≈1 mg (calcd)	microwave heating of acidified MnO_4^- solution	yes	random *versus* assembled MnO_2 nanowires
urchin-like MnO_2 nanospheres[24]	120 F/g (5 mV/s) 80 F/g (200 mV/s)	not shown	0.2 mg/cm^2	hydrothermal	yes	urchin-like to clew-like morphology control
MnO_2 nanowires coated with MnO_2 nanofibrils (this research)	**1.5 μm long nanowires** 377 F/g (50 mV/s) 244 F/g (1000 mV/s)	89.6% after 1000 cycles (91.2% after first 100 cycles)	0.035 mg	two-step electrochemical deposition	no	can control length and diameter of nanowires, and amount of nanofibrils
	4.5 μm long nanowires 298 F/g (50 mV/s) 44 F/g (1000 mV/s)	85.2% after 1000 cycles (86.6% after first 100 cycles)	0.105 mg			

aqueous and acetonitrile solvents. However, this enhancement is shown to result in different mechanisms depending on the solvent. In aqueous solvent, the nanofibril structure increases its capacitance by capacitive processes, while in an acetonitrile solvent, the nanofibril structure increases its capacitance by insertion processes. These results indicate that the solvent has a major effect on whether this material can reach its theoretical capacitance.

At fast scan rates, this hierarchical material showed a good capacitance of 298 F/g at 50 mV/s. The capacitance and power capability was shown to be further improved at the detriment of areal capacitance to 329 F/g at 250 mV/s when the length of the nanowire was shortened from 4.5 to 1.5 μm. The overall hierarchical capacitance was also shown to be improved by smaller diameter nanowires (298 to 375 F/g at 50 mV/s); however, the capacitance attributed to the nanofibrils remains close to the same (572 to 560 F/g) regardless of nanowire diameter. The loading amount of nanofibrils is also shown to have a dynamic affect on the material's specific capacitance with an increase occurring initially due to the high nanofibril surface area followed by a decrease occurring due to the blockage of electrolyte by the increasingly dense nanofibril layer.

This facile synthesis method was successfully applied to other divalent metal solutions (Ni^{2+} and Co^{2+}) resulting in $Ni(OH)_2$ and $Co(OH)_2$ nanofibrils, respectively, conformally coating the MnO_2 nanowires. We hope to analyze these materials in-depth as previous literature has shown great supercapacitor properties with these types of hierarchical/heterogeneous materials.[51,52] Other hierarchical nanostructures are thought to be possible including but not limited to MnO_2/RuO_2, MnO_2/Fe_3O_4, and MnO_2/Al_2O_3 materials from using Ru^{3+}, Fe^{2+}, or Al^{3+} solutions, respectively. This method of formation is versatile enough that it may well be used in the many different applications where MnO_2 is already or proposed to be employed.

METHODS

Chemicals and Materials. All chemicals were purchased with high purity requiring no need for further purification. Manganese acetate, nickel chloride, cobalt chloride, lithium perchlorate, sodium chloride, potassium hydroxide, battery-grade acetonitrile, and sodium hydroxide were purchased from Sigma Aldrich (St. Louis, MO). Deionized water (about 18 MΩ cm^{-1} in resistivity) was made by a Milli-Q water purification system (Millipore; Billerica, MA). Porous anodized aluminum oxide (AAO) membranes of 200 nm in pore diameter and 60 μm in thickness are commercially available from Whatman (Maidstone, Kent, UK), while membranes with 80 nm pore diameters and 50 μm thickness are available from Synkera (Longmont, CO).

Synthesis. *Synthesis of Freestanding MnO_2 Nanowire Array.* This synthesis is represented by Figure 1a. First, a Denton Desk III sputter machine is used to sputter a ≈300 nm gold layer on the branched side of an AAO membrane. A strip of copper tape, to provide good electrical contact, is then attached to the gold side of the membrane. This piece is then sandwiched between layers of Parafilm with part of the nonsputtered side exposed with a defined window of 0.2 cm^2 resulting in completion of the working electrode.

The working electrode is then placed in a 100 mM manganese acetate bath with a Ag/AgCl reference and a platinum counter electrode. A constant voltage of 0.60 V *vs* Ag/AgCl is applied until the total charge passed was 750 mC/cm^2 for 4.5 μm long MnO_2 nanowires or 250 mC/cm^2 for 1.5 μm long nanowires. A soaking time of 30 min in a 3 M solution of sodium hydroxide resulted in the complete dissolution of the alumina membrane, producing vertically aligned MnO_2 nanowires attached to a gold current collector.

Synthesis of MnO_2, $Ni(OH)_2$, and $Co(OH)_2$ Nanofibril/Nanowire Arrays. A MnO_2 nanowire array with a defined window of 0.32 cm^2 is submerged into a 100 mM manganese acetate, nickel chloride, or cobalt chloride bath with a Ag/AgCl reference and a platinum counter electrode. A voltage of −0.85 V *vs* Ag/AgCl was then applied until various amounts of charge were passed. Subsequently, sweeping the potential to 1.0 V *vs* Ag/AgCl resulted in the synthesis of the MnO_2 nanofibril/nanowire array.

Characterization. *Electron Microscopy.* Imaging of the hierarchical MnO_2 nanomaterial was done using a scanning electron microscope (Hitachi SU-70 FEG-SEM) and a transmission electron microscope (JEM 2100 FE-TEM).

Electrochemical Measurements. All of the electrochemical testing was done utilizing a bipotentiostat (BI-STAT, Princeton Applied Research) in a three-electrode configuration. The working electrode consisted of as-deposited freestanding bare MnO_2 nanowire arrays and hierarchical MnO_2 nanofibril/nanowire arrays on a gold current collector. A Ag/AgCl electrode was used as the reference electrode, and a platinum foil was used as the counter electrode. Electrochemical testing was done in both an aqueous and an organic acetonitrile 1 M $LiClO_4$ solution. All capacitance values were obtained using the data from the cyclic voltammetry curves and the following equation:

$$\frac{\int_0^1 I dV}{\upsilon \times \text{mass}} \tag{7}$$

where I is the current, V is the voltage *vs* Ag/AgCl, υ is the scan rate, and mass is the mass of the material.

Inductively Coupled Plasma-Atomic Emission Spectroscopy (ICP-AES). ICP-AES measurements were performed using a PerkinElmer ICP-Optima 4700. Intensities were measured at 257.610 nm for Mn and 231.604 nm for Ni. Calibration curves were made from Mn and Ni standards traceable to the National Institute of Standards and Technology (NIST). All electrodes were dissolved in 3:1 concentrated HCl/HNO_3 and diluted to a known volume before being administered to the plasma.

Raman Spectroscopy. A Horiba Jobin-Yvon LabRAM HR-VIS microRaman system was used to characterize these manganese oxide materials along with MnO, Mn_3O_4, Mn_2O_3, and MnO_2 standards purchased from Sigma-Aldrich. The green line (514.5 nm) of an argon laser was utilized to excite the sample using a spot size of ≈1 μm^2. The spectrum was taken between the Raman shifts of 300 and 900 cm^{-1}.

Electron Energy Loss Spectroscopy. MnO_2, Mn_2O_3, and Mn_3O_4 standards were purchased from Sigma-Aldrich. These standards were each ground with a mortar and pestle in methanol and drop cast on a holey carbon TEM grid.

The MnO_x nanowire samples were grown in AAO by the method above; however, before dissolving the AAO, the electrode was placed in a solution of Mn^{2+} and reduced at 0.85 V *vs* Ag/AgCl until a charge of 100 mC/cm^2 was passed (Supporting Information Figure S3a).

The resulting nanowires were then released from the AAO template using 3 M NaOH for 12 min. These nanowires were then placed on a holey carbon TEM grid.

A field emission gun-transmission electron microscope (FEG-TEM) JEOL JEM 2100F TEM/STEM was used with a Gatan electron energy loss spectrometer to obtain the EELS spectrum.

X-ray Photoelectron Spectroscopy (XPS). XPS analysis was done on a Kratos AXIS 165 spectrometer. The C1s peak was calibrated to 284.8 eV. CasaXPS software was used to obtain the components for the fitted curves.

Conflict of Interest: The authors declare no competing financial interest.

Acknowledgment. The work was supported by the Science of Precision Multifunctional Nanostructures for Electrical Energy Storage (NEES), an Energy Frontier Research Centre funded by the U.S. Department of Energy, Office of Science, Office of Basic Energy Sciences under Award Number DESC0001160. S.B.L. thanks the WCU program by the KOSEF under the MEST (Grant No. R31-2008-000-10071-0). We thank L. Lai and W.A. Chiou (NISP lab) for their help with the TEM imaging and EELS analysis. We are grateful to G. Rubloff for his assistance with the ICP-AES instrumentation. We also appreciate professors R. Penner, P. Collins, and Z. Siwy from UC Irvine for their helpful input during discussion of this work. Finally, we thank K. Gaskell for her help with the XPS results.

Supporting Information Available: Linear sweep voltammetry graph is shown of a MnO_2 nanowire array and bare gold nanoelectrode array to negative potentials, indicating potentials at which MnO_2 and water reduction occur. Figure showing the Raman spectra of MnO, Mn_3O_4, Mn_2O_3, and MnO_2 standards. Side-view SEM images of MnO_2 reduced in Mn^{2+} and Li^+ solutions while embedded in the AAO template. ICP-AES elemental analysis graphs of manganese oxide nanowires and nanofibrils produced in this article. A table of values that includes the capacitance at different scan rates for the bare and hierarchical material in the different solvents. This material is available free of charge *via* the Internet at http://pubs.acs.org.

REFERENCES AND NOTES

1. Perez-Ramirez, J.; Christensen, C. H.; Egeblad, K.; Christensen, C. H.; Groen, J. C. Hierarchical Zeolites: Enhanced Utilisation of Microporous Crystals in Catalysis by Advances in Materials Design. *Chem. Soc. Rev.* **2008**, *37*, 2530–2542.
2. Gao, S. Y.; Yang, S. X.; Shu, J.; Zhang, S. X.; Li, Z. D.; Jiang, K. Green Fabrication of Hierarchical CuO Hollow Micro/Nanostructures and Enhanced Performance as Electrode Materials for Lithium-Ion Batteries. *J. Phys. Chem. C* **2008**, *112*, 19324–19328.
3. Zheng, F. L.; Li, G. R.; Ou, Y. N.; Wang, Z. L.; Su, C. Y.; Tong, Y. X. Synthesis of Hierarchical Rippled Bi_2O_3 Nanobelts for Supercapacitor Applications. *Chem. Commun.* **2010**, *46*, 5021–5023.
4. Sauvage, F.; Di Fonzo, F.; Bassi, A. L.; Casari, C. S.; Russo, V.; Divitini, G.; Ducati, C.; Bottani, C. E.; Comte, P.; Graetzel, M. Hierarchical TiO_2 Photoanode for Dye-Sensitized Solar Cells. *Nano Lett.* **2010**, *10*, 2562–2567.
5. Song, J.; Jensen, D. S.; Hutchison, D. N.; Turner, B.; Wood, T.; Dadson, A.; Vail, M. A.; Linford, M. R.; Vanfleet, R. R.; Davis, R. C. Carbon-Nanotube-Templated Microfabrication of Porous Silicon-Carbon Materials with Application to Chemical Separations. *Adv. Funct. Mater.* **2011**, *21*, 1132–1139.
6. Liu, J. Y.; Guo, Z.; Meng, F. L.; Jia, Y.; Luo, T.; Li, M. Q.; Liu, J. H. Novel Single-Crystalline Hierarchical Structured ZnO Nanorods Fabricated *via* a Wet-Chemical Route: Combined High Gas Sensing Performance with Enhanced Optical Properties. *Cryst. Growth Des.* **2009**, *9*, 1716–1722.
7. Le, V. T.; Le, T. N. L.; Nguyen, V. H. Comparative Study of Gas Sensor Performance of SnO_2 Nanowires and Their Hierarchical Nanostructures. *Sens. Actuators, B* **2010**, *150*, 112–119.
8. Cheng, F. Y.; Zhao, J. Z.; Song, W.; Li, C. S.; Ma, H.; Chen, J.; Shen, P. W. Facile Controlled Synthesis of MnO_2 Nanostructures of Novel Shapes and Their Application in Batteries. *Inorg. Chem.* **2006**, *45*, 2038–2044.
9. Ding, Y. S.; Shen, X. F.; Gomez, S.; Luo, H.; Aindow, M.; Suib, S. L. Hydrothermal Growth of Manganese Dioxide into Three-Dimensional Hierarchical Nanoarchitectures. *Adv. Funct. Mater.* **2006**, *16*, 549–555.
10. Fei, J. B.; Cui, Y.; Yan, X. H.; Qi, W.; Yang, Y.; Wang, K. W.; He, Q.; Li, J. B. Controlled Preparation of MnO_2 Hierarchical Hollow Nanostructures and Their Application in Water Treatment. *Adv. Mater.* **2008**, *20*, 452–456.
11. Hasan, H. *Manganese*, 1st ed.; Rosen Central: New York, 2008; p 48.
12. Xu, C. J.; Kang, F. Y.; Li, B. H.; Du, H. D. Recent Progress on Manganese Dioxide Based Supercapacitors. *J. Mater. Res.* **2010**, *25*, 1421–1432.
13. Emsley, J. *Nature's Building Blocks: An A–Z Guide to the Elements*; Oxford University Press: New York, 2001; p 538.
14. Chabre, Y.; Pannetier, J. Structural and Electrochemical Properties of the Proton γ-MnO_2 System. *Prog. Solid State Chem.* **1995**, *23*, 1–130.
15. Wang, H. L.; Cui, L. F.; Yang, Y. A.; Casalongue, H. S.; Robinson, J. T.; Liang, Y. Y.; Cui, Y.; Dai, H. J. Mn_3O_4-Graphene Hybrid as a High-Capacity Anode Material for Lithium Ion Batteries. *J. Am. Chem. Soc.* **2010**, *132*, 13978–13980.
16. Reddy, A. L. M.; Shaijumon, M. M.; Gowda, S. R.; Ajayan, P. M. Coaxial MnO_2/Carbon Nanotube Array Electrodes for High-Performance Lithium Batteries. *Nano Lett.* **2009**, *9*, 1002–1006.
17. Ammundsen, B.; Paulsen, J. Novel Lithium-Ion Cathode Materials Based on Layered Manganese Oxides. *Adv. Mater.* **2001**, *13*, 943–956.
18. Liu, R.; Lee, S. B. MnO_2/Poly(3,4-ethylenedioxythiophene) Coaxial Nanowires by One-Step Coelectrodeposition for Electrochemical Energy Storage. *J. Am. Chem. Soc.* **2008**, *130*, 2942–2943.
19. Toupin, M.; Brousse, T.; Belanger, D. Influence of Microstucture on the Charge Storage Properties of Chemically Synthesized Manganese Dioxide. *Chem. Mater.* **2002**, *14*, 3946–3952.
20. Hu, C. C.; Tsou, T. W. Ideal Capacitive Behavior of Hydrous Manganese Oxide Prepared by Anodic Deposition. *Electrochem. Commun.* **2002**, *4*, 105–109.
21. Yan, W. B.; Ayvazian, T.; Kim, J.; Liu, Y.; Donavan, K. C.; Xing, W. D.; Yang, Y. G.; Hemminger, J. C.; Penner, R. M. Mesoporous Manganese Oxide Nanowires for High-Capacity, High-Rate, Hybrid Electrical Energy Storage. *ACS Nano* **2011**, *5*, 8275–8287.
22. Conway, B. E.; Birss, V.; Wojtowicz, J. The Role and Utilization of Pseudocapacitance for Energy Storage by Supercapacitors. *J. Power Sources* **1997**, *66*, 1–14.
23. Li, Z. Q.; Ding, Y.; Xiong, Y. J.; Yang, Q.; Xie, Y. One-Step Solution-Based Catalytic Route To Fabricate Novel α-MnO_2 Hierarchical Structures on a Large Scale. *Chem. Commun.* **2005**, 918–920.
24. Yu, P.; Zhang, X.; Wang, D. L.; Wang, L.; Ma, Y. W. Shape-Controlled Synthesis of 3D Hierarchical MnO_2 Nanostructures for Electrochemical Supercapacitors. *Cryst. Growth Des.* **2009**, *9*, 528–533.
25. Jiang, J.; Li, Y. Y.; Liu, J. P.; Huang, X. T.; Yuan, C. Z.; Lou, X. W. Recent Advances in Metal Oxide-Based Electrode Architecture Design for Electrochemical Energy Storage. *Adv. Mater.* **2012**, *24*, 5166–5180.
26. Xu, C. L.; Bao, S. J.; Kong, L. B.; Li, H.; Li, H. L. Highly Ordered MnO_2 Nanowire Array Thin Films on Ti/Si Substrate as an Electrode for Electrochemical Capacitor. *J. Solid State Chem.* **2006**, *179*, 1351–1355.
27. Kim, J. H.; Ayalasomayajula, T.; Gona, V.; Choi, D. Fabrication and Electrochemical Characterization of a Vertical Array of MnO_2 Nanowires Grown on Silicon Substrates as a Cathode Material for Lithium Rechargeable Batteries. *J. Power Sources* **2008**, *183*, 366–369.
28. Linden, D.; Reddy, T. B. *Handbook of Batteries*, 3rd ed.; McGraw-Hill: New York, 2002; section 10.4.
29. Pourbaix, M. *Atlas of Electrochemical Equilibria in Aqueous Solutions*, 2nd English ed.; National Association of Corrosion Engineers: Houston, TX, 1974; p 644.
30. Bricker, O. Some Stability Relations in System Mn-O_2-H_2O at 25 Degrees and 1 atm Total Pressure. *Am. Mineral.* **1965**, *50*, 1296–1354.
31. Julien, C.; Massot, M.; Baddour-Hadjean, R.; Franger, S.; Bach, S.; Pereira-Ramos, J. P. Raman Spectra of Birnessite

Manganese Dioxides. *Solid State Ionics* **2003**, *159*, 345–356.
32. Hsu, Y. K.; Chen, Y. C.; Lin, Y. G.; Chen, L. C.; Chen, K. H. Reversible Phase Transformation of MnO_2 Nanosheets in an Electrochemical Capacitor Investigated by *In Situ* Raman Spectroscopy. *Chem. Commun.* **2011**, *47*, 1252–1254.
33. Bernard, M. C.; Goff, A. H. L.; Thi, B. V.; Detorresi, S. C. Electrochromic Reactions in Manganese Oxides 0.1. Raman Analysis. *J. Electrochem. Soc.* **1993**, *140*, 3065–3070.
34. Grunes, L. A.; Leapman, R. D.; Wilker, C. N.; Hoffmann, R.; Kunz, A. B. Oxygen-K Near-Edge Fine-Structure: An Electron-Energy-Loss Investigation with Comparisons to New Theory for Selected 3D Transition-Metal Oxides. *Phys. Rev. B: Condens. Matter Mater. Phys.* **1982**, *25*, 7157–7173.
35. Kurata, H.; Lefevre, E.; Colliex, C.; Brydson, R. Electron-Energy-Loss Near-Edge Structures in the Oxygen K-Edge Spectra of Transition-Metal Oxides. *Phys. Rev. B: Condens. Matter Mater. Phys.* **1993**, *47*, 13763–13768.
36. Audi, A. A.; Sherwood, P. M. A. Valence-Band X-ray Photoelectron Spectroscopic Studies of Manganese and Its Oxides Interpreted by Cluster and Band Structure Calculations. *Surf. Interface Anal.* **2002**, *33*, 274–282.
37. Grosvenor, A. P.; Biesinger, M. C.; Smart, R. S.; McIntyre, N. S. New Interpretations of XPS Spectra of Nickel Metal and Oxides. *Surf. Sci.* **2006**, *600*, 1771–1779.
38. Yang, J.; Liu, H. W.; Martens, W. N.; Frost, R. L. Synthesis and Characterization of Cobalt Hydroxide, Cobalt Oxyhydroxide, and Cobalt Oxide Nanodiscs. *J. Phys. Chem. C* **2010**, *114*, 111–119.
39. Liu, T. C.; Pell, W. G.; Conway, B. E.; Roberson, S. L. Behavior of Molybdenum Nitrides as Materials for Electrochemical Capacitors: Comparison with Ruthenium Oxide. *J. Electrochem. Soc.* **1998**, *145*, 1882–1888.
40. Wang, J.; Polleux, J.; Lim, J.; Dunn, B. Pseudocapacitive Contributions to Electrochemical Energy Storage in TiO_2 (Anatase) Nanoparticles. *J. Phys. Chem. C* **2007**, *111*, 14925–14931.
41. Ardizzone, S.; Fregonara, G.; Trasatti, S. Inner and Outer Active Surface of RuO_2 Electrodes. *Electrochim. Acta* **1990**, *35*, 263–267.
42. Depauli, C. P.; Trasatti, S. Electrochemical Surface Characterization of IrO_2+SnO_2 Mixed-Oxide Electrocatalysts. *J. Electroanal. Chem.* **1995**, *396*, 161–168.
43. Toupin, M.; Brousse, T.; Belanger, D. Charge Storage Mechanism of MnO_2 Electrode Used in Aqueous Electrochemical Capacitor. *Chem. Mater.* **2004**, *16*, 3184–3190.
44. Qu, Q. T.; Zhang, P.; Wang, B.; Chen, Y. H.; Tian, S.; Wu, Y. P.; Holze, R. Electrochemical Performance of MnO_2 Nanorods in Neutral Aqueous Electrolytes as a Cathode for Asymmetric Supercapacitors. *J. Phys. Chem. C* **2009**, *113*, 14020–14027.
45. Xu, M.; Kong, L.; Zhou, W.; Li, H. Hydrothermal Synthesis and Pseudocapacitance Properties of α-MnO_2 Hollow Spheres and Hollow Urchins. *J. Phys. Chem. C* **2007**, *111*, 19141–19147.
46. Tang, X. H.; Liu, Z. H.; Zhang, C. X.; Yang, Z. P.; Wang, Z. L. Synthesis and Capacitive Property of Hierarchical Hollow Manganese Oxide Nanospheres with Large Specific Surface Area. *J. Power Sources* **2009**, *193*, 939–943.
47. Li, Z. P.; Wang, J. Q.; Wang, Z. F.; Ran, H. Q.; Li, Y.; Han, X. X.; Yang, S. R. Synthesis of a Porous Birnessite Manganese Dioxide Hierarchical Structure Using Thermally Reduced Graphene Oxide Paper as a Sacrificing Template for Supercapacitor Application. *New J. Chem.* **2012**, *36*, 1490–1495.
48. Hu, C. C.; Hung, C. Y.; Chang, K. H.; Yang, Y. L. A Hierarchical Nanostructure Consisting of Amorphous MnO_2, Mn_3O_4 Nanocrystallites, and Single-Crystalline Mnooh Nanowires for Supercapacitors. *J. Power Sources* **2011**, *196*, 847–850.
49. Sumboja, A.; Tefashe, U. M.; Wittstock, G.; Lee, P. S. Monitoring Electroactive Ions at Manganese Dioxide Pseudocapacitive Electrodes with Scanning Electrochemical Microscope for Supercapacitor Electrodes. *J. Power Sources* **2012**, *207*, 205–211.
50. Meher, S. K.; Rao, G. R. Enhanced Activity of Microwave Synthesized Hierarchical MnO_2 for High Performance Supercapacitor Applications. *J. Power Sources* **2012**, *215*, 317–328.
51. Liu, J. P.; Jiang, J.; Bosman, M.; Fan, H. J. Three-Dimensional Tubular Arrays of MnO_2-NiO Nanoflakes with High Areal Pseudocapacitance. *J. Mater. Chem.* **2012**, *22*, 2419–2426.
52. Liu, J. P.; Jiang, J.; Cheng, C. W.; Li, H. X.; Zhang, J. X.; Gong, H.; Fan, H. J. Co_3O_4 Nanowire@MnO_2 Ultrathin Nanosheet Core/Shell Arrays: A New Class of High-Performance Pseudocapacitive Materials. *Adv. Mater.* **2011**, *23*, 2076–2081.